Energy & Environmental Science

RSC Publishing

PAPER

View Article Online
View Journal | View Issue

Cite this: *Energy Environ. Sci.*, 2013, **6**, 3713

Modeling an integrated photoelectrolysis system sustained by water vapor

Chengxiang Xiang,† Yikai Chen† and Nathan S. Lewis*

Two designs for an integrated photoelectrolysis system sustained by water vapor have been investigated using a multi-physics numerical model that accounts for charge and species conservation, electron and ion transport, and electrochemical processes. Both designs leverage the use of a proton-exchange membrane that provides conductive pathways for reactant/product transport and prevents product crossover. The resistive losses, product gas transport, and gas crossovers as a function of the geometric parameters of the two designs have been evaluated systematically. In these designs, minimization of pathways in the membrane that can support the diffusive transport of product gases from the catalyst to the gas-collecting chamber was required to prevent supersaturation of hydrogen or oxygen gases at the Nafion/catalyst interface. Due to the small, thin membrane layer that was required, a small electrode width (<300 μm) was also required to produce low resistive losses in the system. Alternatively, incorporation of a structured membrane that balances the gas transport and ionic transport allows the maximum electrode width to be increased to dimensions as large as a few millimeters. Diffusive gas transport between the cathode and anode was the dominant source for crossover of the product gases under such circumstances. The critical dimension of the electrode required to produce acceptably low rates of product crossover was also investigated through the numerical modeling and device simulations.

Received 26th June 2013
Accepted 20th September 2013

DOI: 10.1039/c3ee42143k

www.rsc.org/ees

Broader context

An integrated solar-driven water-splitting cell has the potential for large-scale solar energy conversion and storage. The design principles and operational details of the cell depend on the system input feedstock. Most studies use the liquid electrolyte as a feedstock, where strong acid and strong base are typically employed to reduce the resistive loss in the system. The use of water vapor or pure water as the feedstock has several potential advantages, which can benefit large-scale implementation of a photoelectrolysis system. In this paper, we addressed some unique challenges and studied the design criteria for such a system by a multi-physics numerical model that accounts for charge and species conservation, electron and ion transport, and electrochemical processes.

I. Introduction

An integrated photoelectrolysis system in which light absorbers, electrocatalysts and membrane separators are integrated together efficiently, scalably and robustly is an interesting option for solar energy conversion and storage applications.[1–3] The fundamental properties, design principles, and operational details of the individual components in such an integrated system have been recently evaluated in detail.[4–11] To facilitate operation at high current densities (>1 A cm^{-2} at 80–90 °C) and thus optimize the balance of systems cost,[12,13] electrolytes based on the use of liquid water as a feed are employed exclusively in electrolyzers. However, an integrated solar-driven water-splitting system can in principle use gaseous water vapor as the feed stock, because the water vapor content of humid air is generally sufficient to provide the needed water flux under many circumstances to support the solar-generated photon flux, and corresponding product flux, that will be produced by a light-limited current density of 10–20 mA cm^{-2} typically obtained under unconcentrated sunlight.[14,15]

The use of water vapor as the system input feedstock has several potential advantages as compared to a traditional device that contains a liquid electrolyte. A water vapor device would mitigate deleterious effects associated with bubble formation during operation, including blocking of active electrocatalytic sites, scattering or reflection of incident illumination away from the light absorbers, *etc.*[14,16–19] The thermodynamic potential for the water-splitting reaction is also more favorable for gaseous water than for liquid water, because the electrolysis of liquid water ($E^0[H_2O(l)] = 1.229$ V) requires an additional ~44 mV as compared to the electrolysis of water vapor ($E^0[H_2O(g)] = 1.185$ V).[20]

The use of $H_2O(g)$ as a feed to an integrated photoelectrolysis system presents, however, some unique challenges with respect

Beckman Institute, Kavli Nanoscience Institute, and Joint Center for Artificial Photosynthesis, Division of Chemistry and Chemical Engineering, California Institute of Technology, Pasadena, CA 91125, USA. E-mail: nslewis@caltech.edu

† These authors contributed equally to this work.

to ionic transport and product gas transport. The membrane is most likely to be in direct physical contact with the electrocatalysts, with the opposite side of the electrocatalyst being a solid piece of photoabsorber. To prevent delamination of the membrane at the interface, the hydrogen or oxygen produced at the electrocatalyst/membrane interface would therefore have to diffuse through the membrane without formation of bubbles. Spurgeon, *et al.*[21] performed a proof-of-concept study on a water electrolysis system sustained by water vapor by operating a commercially available, membrane-based fuel cell unit in reverse, with the reaction driving force provided by an external power supply. Electrically driven water-electrolysis systems generally utilize a membrane-electrode-assembly to optimize the electrical, proton and gas transport. However, in an integrated photoelectrolysis system, the introduction of a light-capturing element, the photoabsorber, will significantly alter the optimal design parameters of the system. Haussener, *et al.*,[6,7] have presented optimal design parameters and materials properties for two characteristic photoelectrochemical devices, both of which operate in 1 M H_2SO_4(aq). However, the engineering-design aspects that are related to the transport phenomena have yet to be investigated for a system based on a H_2O(g) feed.

In this work, two characteristic cell designs that use a proton exchange membrane and that exhibit low resistive loss (<100 mV), facile gas transport, and minimal gas crossover while in operation (10 mA cm^{-2}) have been evaluated in detail. The first cell design uses a thin, membrane enclosed, micro-scale photoabsorber (critical dimension < 300 μm) and represents an approach in which the ionic pathway between the cathode and the anode, and the diffusive pathway for the gas transport in membrane from the catalyst to the gas-collecting chamber, are both minimized. The second cell design features a structured membrane enclosed by mm-scale photoabsorbers, and represents a situation in which the ionic pathways and gas transport are optimized separately, by adjusting the proton transport channel and the gas transport channel in the system. Simulations of product crossover in micro-sized electrodes have also been performed, and these results indicate that the use of a proton-exchange membrane, such as Nafion, inherently minimizes the product crossover in such systems.

II. Modeling

A. Governing equations

The ionic transport in a proton-exchange membrane, *e.g.*, Nafion, is governed by Ohm's law:

$$i_l = \sigma_l \nabla \phi_l,$$

where σ_l is the electrolyte conductivity, ϕ_l is the electrolyte potential and i_l is the ionic current. Assuming dilute-solution theory, in which the interactions among the solutes are not rigorously considered, the electrolyte conductivity can be derived from the Nernst–Planck equation, yielding:[22]

$$\sigma_l = \frac{F^2}{RT} \sum_i z_i^2 D_i c_i$$

where c_i is the concentration of species i, D_i is the diffusion coefficient of species i, z_i is the charge number of the ionic species, and F is Faraday's constant.

The kinetics of the 4-electron transfer oxygen-evolution reaction (OER) and the 2-electron transfer hydrogen-evolution reaction (HER) at the electrode/membrane interface are approximated by the Butler–Volmer equations.[20]

$$i_{R,OER/HER} = i_{0,OER/HER}\left[\exp\left(\frac{\alpha_{a,OER/HER} F\eta}{RT}\right) - \exp\left(-\frac{\alpha_{c,OER/HER} F\eta}{RT}\right)\right],$$

where $i_{0,OER}$ and $i_{0,HER}$ are the respective exchange-current densities, $\alpha_{a,OER}$ and $\alpha_{a,HER}$ are the transfer coefficients for the OER and HER, respectively, and η is the overpotential, which is defined as

$$\eta = \phi_s - \phi_l - \phi_0,$$

where ϕ_s and ϕ_l are the electric and electrolyte potential at the electrode-electrolyte interface, respectively, and ϕ_0 is the equilibrium potential. The value of ϕ_0 was set to $\phi_0 = 0.0$ V for the cathode and to 1.185 V for the anode. The conservation of charge and the continuity of current density were also employed at the electrode/membrane interface.[22]

The transport of gaseous products in Nafion is also governed by the Nernst–Planck equation. Assuming a zero velocity field, the governing equation reduces to Fick's second law at steady state:

$$0 = D_i \nabla^2 C_i,$$

where C_i is the concentration and D_i the diffusion coefficient of dissolved hydrogen or oxygen in Nafion.

B. Cell designs

Fig. 1 shows schematic illustrations of the two cell designs that were evaluated for performance during operation while fed by water vapor. Both designs are illustrated in 2-D cross-sections, with the out-of-the-plane dimension assumed to be infinite. In Design A (Fig. 1a), the photoelectrolysis assembly contained a photocathode, a photoanode and electrocatalysts, all embedded in a proton-exchange membrane (*e.g.*, Nafion). The fill fraction, defined as the ratio between the light-capturing geometric area and the total area of the cell, was determined by the ratio between the electrode width, l_e and the cell width, l_c. The Nafion film supports ionic transport between the anode and the cathode, and also supports product gas transport from the electrocatalysts to the gas-collecting chamber (not indicated). In Design B (Fig. 2b), the photoelectrolysis assembly was embedded in a structured Nafion film, with gas channels and Nafion channels introduced into the cell. Thin Nafion underlayers (0.5 μm) that were coated on top of the catalyst layers provided facile gas transport to the gas channels. The Nafion channels in between the gas channels provided low resistance pathways for ionic transport between the cathode and anode. Thick Nafion overlayers were further employed as required to meet specified design considerations, and served to decrease the resistive losses in the cell.

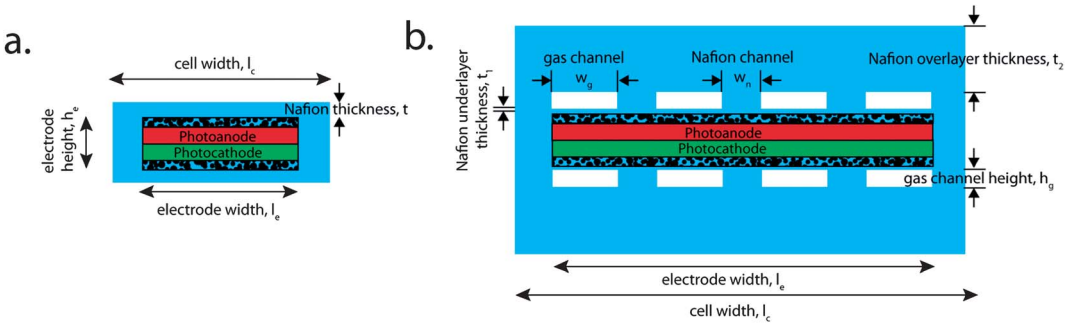

Fig. 1 Schematic illustrations of two cell designs for a photoelectrolysis device sustained by a water vapor feed. Both designs contain a photocathode (red), a photoanode (green), electrocatalyst layers (dotted) and Nafion film (blue) used as a representative solid polymer electrolyte material. In Design A, the electrode width, electrode height, cell width and Nafion thickness are labeled as l_e, h_e, l_c and t, respectively. In Design B, the gas channel width, gas channel height, Nafion channel width, Nafion underlayer thickness and Nafion overlayer thickness are labeled as w_g, h_g, w_n, t_1, and t_2, respectively.

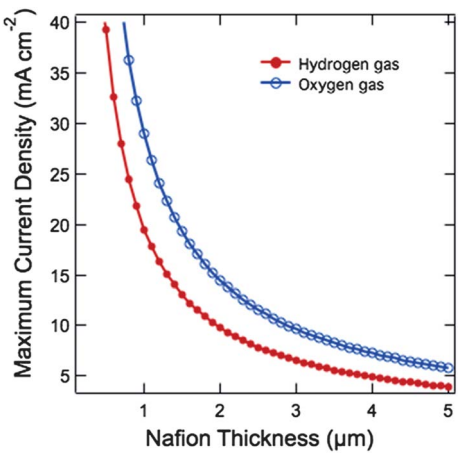

Fig. 2 Maximum sustainable current density, as a function of the Nafion thickness, allowed to avoid supersaturation of oxygen (blue) or hydrogen (red) at the Nafion/catalyst interface in Design A.

C. Model parameters

Table 1 presents the basic parameters used in the model. In our modeling, the transport of *gaseous products* (hydrogen or oxygen) in Nafion is governed only by diffusion. In contrast, the ion transport and proton transport is governed by Nernst–Planck relation, which includes diffusion, migration and convection terms. Assuming zero convection and using the Nernst–Einstein relation, the Nernst–Planck relation simply reduces to Ohm's law, which provided the basis for calculation of the resistive losses in the system. In all simulations, the Nafion membrane was assumed to be fully hydrated, which can be readily achieved by operating the cell in a sufficiently humidified atmosphere.[21] In the simulation of the resistive losses, symmetry boundary conditions for the current densities were used for the vertical walls of both designs. Insulating boundary conditions were applied at the upper and bottom bounds of the Nafion film. A Neumann (or second-type) boundary condition of the current flux (10 mA cm^{-2}) was applied at the electrode surface. The ionic conductivity of the Nafion film was set to 10 S m^{-1} in the subdomain settings. The electrochemical reactions for both designs were modeled as a surface reaction that occurred between the Nafion and the catalytic layer.

In the gas transport simulation, for Design A, a 1-D analytical calculation based on Fick's first law was used to determine the maximum sustainable flux at a given Nafion thickness, with the hydrogen (oxygen) concentrations at the Nafion/catalyst interface and the Nafion/vapor interface set to 0.78 mM (1.23 mM) and 0 mM (0 mM), respectively. For Design B, symmetry boundary conditions for the H_2 or O_2 fluxes were used for the vertical walls. Insulating boundary conditions were applied at the upper and lower bounds of the Nafion film. Neumann (or second-type) boundary conditions of the gas fluxes (equivalent to 10 mA cm^{-2}) were applied at the electrode surface. The Dirichlet (or first-type) boundary condition was applied at the perimeters of the gas channels, where the concentrations of dissolved hydrogen was set to 0 mM, 0.2 mM, 0.4 mM or 0.6 mM for different sweep gas fluxes in the gas channel. The diffusion coefficient of the dissolved hydrogen and oxygen in the Nafion was set to 1.3×10^{-5} cm^2 s^{-1} and 6.1×10^{-6} cm^2 s^{-1}, respectively.

In the crossover simulation, insulating boundary conditions were applied at the upper and bottom bounds of the Nafion

Table 1 Basic parameters used in the model

Electrochemical kinetics[23,24]	OER exchange current density, $i_{R,OER}$	0.00014 mA cm^{-2}
	OER anodic transfer coefficient, $\alpha_{a,OER}$	1.0
	OER cathodic transfer coefficient, $\alpha_{c,OER}$	0.1
	HER exchange current density, $i_{R,HER}$	1 mA cm^{-2}
	HER anodic transfer coefficient, $\alpha_{a,HER}$	2.57
	HER cathodic transfer coefficient, $\alpha_{c,HER}$	2.57
Nafion[25–27]	Diffusivity H_2, D_{H_2}	1.3×10^{-5} cm^2 s^{-1}
	Diffusivity O_2, D_{O_2}	6.1×10^{-6} cm^2 s^{-1}
	Conductivity, σ_l	100 mS cm^{-1}
Operating conditions[28]	Temperature, T	298 K
	Photocurrent density, i_{pc}	10 mA cm^{-2}
	Saturation concentration H_2, $c_{H_2,sat}$	0.78 mM
	Saturation concentration O_2, $c_{O_2,sat}$	1.23 mM

film. The Dirichlet (or first-type) boundary condition was used at the electrode, where the concentration of the dissolved hydrogen was set to the solubility limit (0.78 mM at room temperature). The concentration of dissolved hydrogen was set to zero at the cathode and the anode, respectively, to evaluate the situation for the maximum diffusive crossover condition.

Free triangular discretization and a standard solver in the Comsol multi-physics package were used in the modeling. For Design A, the maximum and minimum mesh element size were set to 10 μm and 0.1 μm, respectively, and the maximum mesh element growth rate and the resolution of curvature were fixed to 1.2 and 0.25, respectively. For Design B, the maximum and minimum mesh element size were set to 100 μm and 1 μm, respectively, and the maximum mesh element growth rate and the resolution of curvature were set at 1.3 and 0.3, respectively. A relative tolerance of the corresponding variable of 0.001 was applied as the convergence criterion for both designs.

III. Results

A. Design A

1. Product gas transport (1-D transport). In Design A, the oxygen and hydrogen transport from the Nafion/catalyst interface to the gas-collecting chamber can be treated as a 1-D diffusive gas transport process. Fig. 2 shows the maximum current density that can be sustained in a 1-D planar geometry without supersaturation of hydrogen or oxygen at the Nafion/catalyst interface, as a function of the thickness of the Nafion film. For the cell to operate at 10 mA cm^{-2} without supersaturation at the Nafion/catalyst interface, the Nafion thickness cannot exceed 1.9 μm for the photocathode side and 2.9 μm for the photoanode side. To ensure sufficient gas transport in the system, the thickness of the Nafion film in Design A was therefore set to 1.9 μm in all subsequent simulations.

2. Resistive losses. In Design A, the conductive pathways in the thin layer Nafion film (~2 μm) are significantly more confined than a liquid-electrolyte based design, for which the electrolyte height is typically on the order of several millimeters.[6] Fig. 3 shows the resistive loss as a function of the normalized lateral position on the photoelectrode, for six electrode widths. A large variation in the resistance drops was observed across the electrode, due to longer ion transport pathways between the mid-point of the photocathode to the mid-point to the photoanode and shorter pathways between the edge points, especially in geometries that had large electrode widths.

Fig. 4 shows the maximum resistive drops along the photoelectrodes as a function of the electrode width. Three electrode heights of the photoelectrode, 1 μm (Fig. 4a), 10 μm (Fig. 4b) and 100 μm (Fig. 4c), were simulated, to account for different types of photoabsorber materials. For each electrode height, three different fill fractions, ff = l_e/l_c, 0.5, 0.9 and 0.98 were also simulated, where l_e is the PV (photovoltaic) electrode width and l_c is the cell width. In all cases, the resistive loss increased as a function of the electrode width, due to increased length of the ionic pathways in the thin Nafion layer. When the electrode height was set to 1 μm, the resistive loss as a function of the electrode width exhibited little dependence on the fill fraction of the design. In contrast, as the electrode height increased, the resistive loss exhibited a stronger dependence on the fill fraction of the design. To minimize the resistive losses to <100 mV, the electrode width should not exceed ~300 μm even with a 1 μm electrode height.

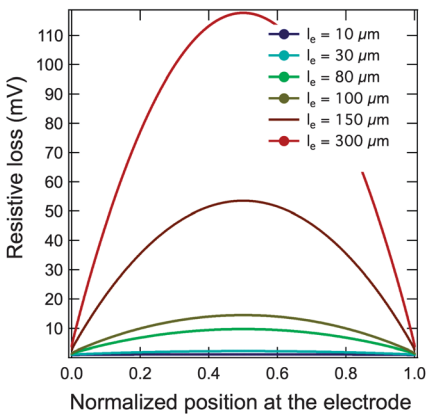

Fig. 3 Resistive loss as a function of normalized position along the electrode for six different electrode widths in Design A.

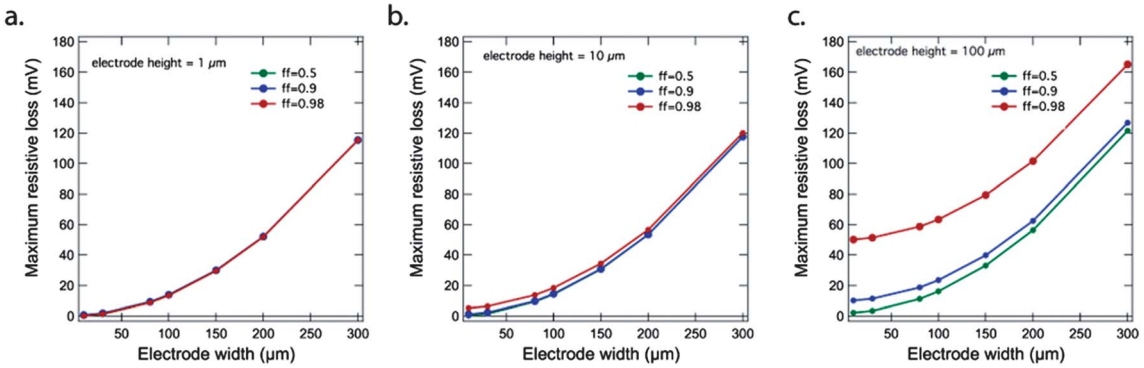

Fig. 4 Maximum resistive loss as a function of the electrode width for three different electrode heights, 1 μm (a), 10 μm (b) and 100 μm (c), in Design A. Three fill fractions, 0.5 (green), 0.9 (blue) and 0.98 (red) were simulated for each electrode width.

B. Design B

1. Product (2-D) gas transport. In Design B, the structured Nafion film provides a balance between the ionic conductivity and gas transport of the products. Because 10 mA cm^{-2} of photocurrent density was generated uniformly along the photoelectrode, the regions directly beneath the Nafion channel would have the longest diffusive pathways. As the width of the Nafion channel decreases, gas transport improves due to the decreased length of pathways for the transport of the product gases. However, a decrease in the Nafion channel width will concomitantly hinder the ion transport and therefore increase the resistive losses in the cell.

Fig. 5a depicts the hydrogen concentration profile in Design B with 10 mA cm^{-2} of photocurrent density generated uniformly at the photoelectrode/Nafion underlayer interface. The simulations indicated that the hydrogen concentration reached its highest value at the mid-point of the Nafion channel along the photoelectrode. In this particular geometry, the highest hydrogen concentration was 0.47 mM, which is still below the saturation concentration of hydrogen in a film of Nafion (0.78 mM).

Fig. 5b shows the maximum hydrogen concentration, which occurred in the mid-point of the Nafion film, as a function of the Nafion channel width, where the gas channel width was set to 50 μm and the hydrogen concentration at the perimeter of the gas channel was set to 0 mM (black), 0.20 mM (blue) or 0.40 mM (red). Fig. 5c shows the maximum hydrogen concentration as a function of the gas channel width for two Nafion channel widths. The maximum hydrogen concentration showed a quasi-linear dependence on the width of the Nafion film, and exhibited no dependence on the width of the gas channel. The simulation results provided an upper bound (5.17 μm, 3.70 μm and 2.13 μm for the hydrogen concentration of 0 mM, 0.20 mM and 0.40 mM, respectively, at the perimeter of the gas channel) for the width of the Nafion channel needed to avoid supersaturation at the Nafion/catalyst interface. Thus, for effective hydrogen transport, a higher sweep gas flux in the gas channel

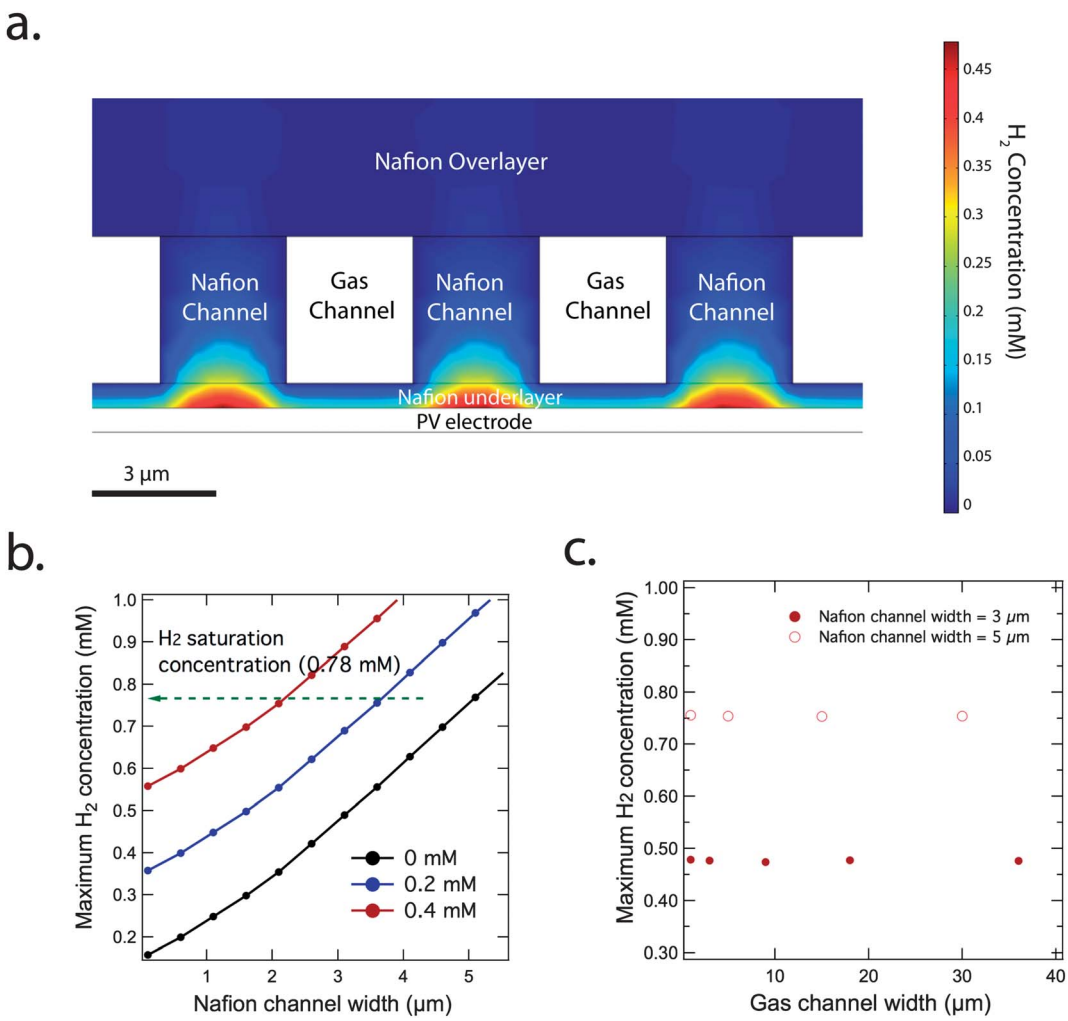

Fig. 5 (a) The hydrogen concentration profile in Design B, where the electrode width, electrode height, Nafion channel width, gas channel width, gas channel height, Nafion underlayer thickness, Nafion overlayer thickness were set to 2.34 mm, 10 μm, 3 μm, 3 μm, 3 μm, 0.5 μm, and 200 μm, respectively. (b) The maximum hydrogen concentration as a function of the Nafion channel width, where the gas channel width was set to 5 μm and the hydrogen concentration at the perimeter of the gas channel was set to 0 mM (black), 0.20 mM (blue) or 0.40 mM (red). (c) The maximum hydrogen concentration as a function of the gas channel width, where the Nafion channel width was set to 3 μm (solid dot) and 5 μm (hollow dot), respectively.

is preferable to achieve a low hydrogen concentration at the perimeter of the gas channels. For a 1 m × 1 m system fed by water vapor, a sweep gas flux of 0.040 mol s^{-1} is required to achieve a 0.010 mM concentration of hydrogen at the perimeter of the gas channel.

2. Resistive losses. In Design B, the ionic pathways consist of three segments connected in series: the Nafion underlayer, the Nafion channel and the Nafion overlayer. The structured Nafion film maximizes the electrode width while maintaining low resistive losses (<100 mV). Fig. 6a shows the electrolyte potential profile in Design B, with the detailed cell geometry provided in the figure caption. As indicated by the trajectory of current density lines in black (Fig. 6a), the Nafion channels served as conductive bridges between the Nafion underlayer and the Nafion overlayer. In this particular geometry, the maximum resistive loss was 108 mV.

Fig. 6b shows the maximum resistive loss as a function of the electrode width for three different Nafion overlayer thicknesses, when the gas channel width was set to zero. Fig. 6b provided an upper bound for the electrode width in Design B, where the conductive pathway between the cathode and anode was optimized. In these limiting cases (Fig. 6b), for a resistive drop of <100 mV, the electrode width cannot exceed 1.7 mm, 2.6 mm and 4.0 mm, respectively, when the Nafion overlayer thickness was set to 100 μm, 200 μm, and 600 μm, respectively.

The best limiting scenario for resistive losses simulated in Fig. 6b did not provide sufficient product gas transport. To prevent supersaturation of product gases at the Nafion/catalyst interfaces, a Nafion channel with a width of <5.17 μm (Fig. 5b) is required. Fig. 6c shows the maximum resistive loss as a function of the Nafion overlayer thickness, when the electrode width and the Nafion channel width were set to 2.34 mm and 5.17 μm, respectively. The maximum resistive loss decreased as the Nafion overlayer thickness increased, and the resistive loss plateaued at a Nafion thickness of ~800 μm. The black curve shows the limiting case scenario in which the gas channel width was set to zero, and served to provide a lower bound for the resistive loss in this particular electrode width (2.34 mm) for

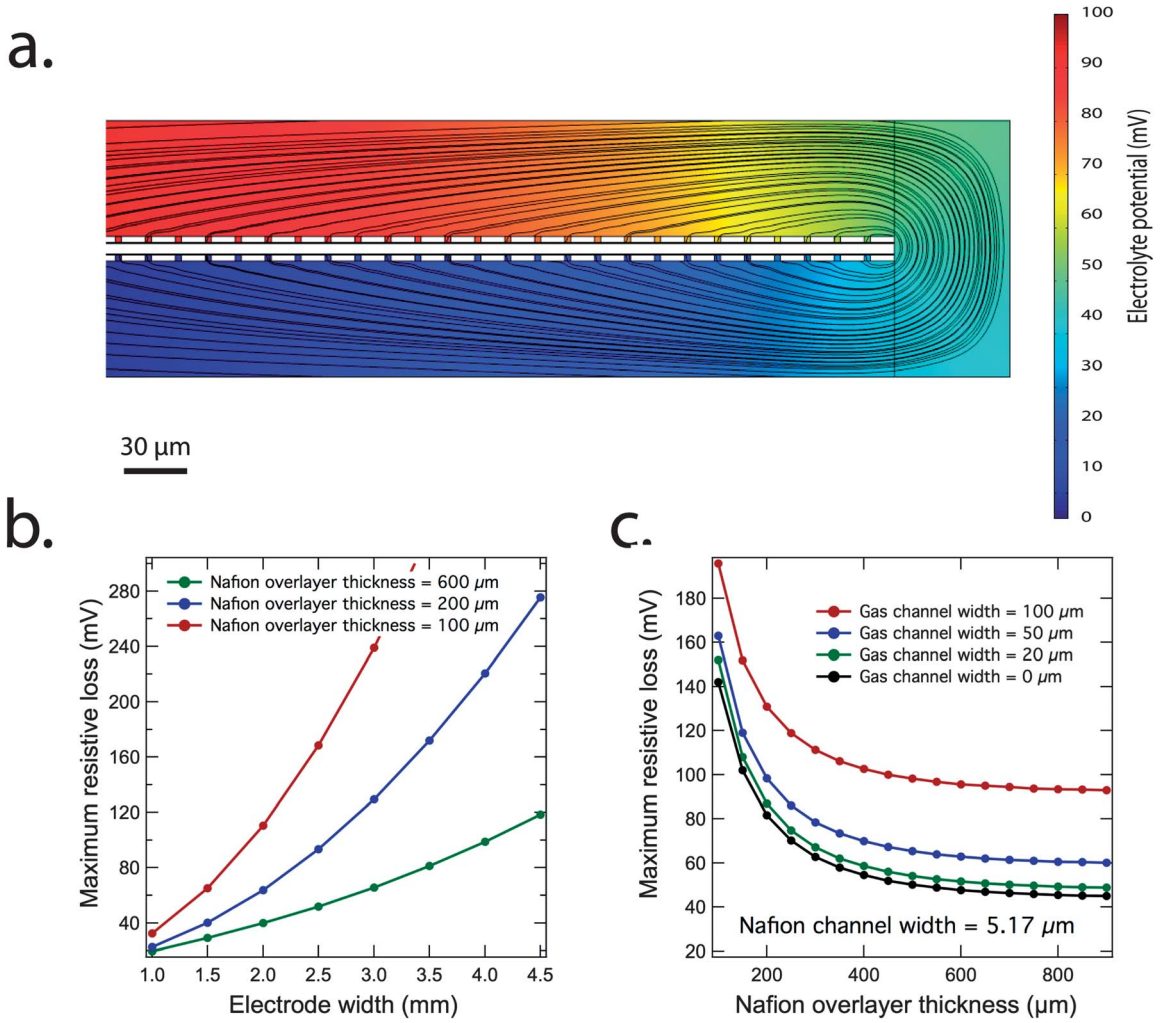

Fig. 6 (a). The electrolyte potential profile in Design B, with the electrode width, electrode height, Nafion channel width, gas channel width, gas channel height, Nafion underlayer thickness, Nafion overlayer thickness were set to 2.34 mm, 10 μm, 5.17 μm, 20 μm, 5.17 μm, 0.5 μm and 150 μm, respectively. (b) The maximum resistive loss a function of the electrode width for three Nafion overlayer thickness, 100 μm (red), 200 μm (blue) and 600 μm (green). (c) The maximum resistive loss as a function of the Nafion overlayer thickness for four different gas channel widths. The electrode width and the Nafion channel height were set to 2.4 mm and 5.17 μm, respectively.

Design B. The resistive loss also showed a strong dependence on the gas channel width. By choosing a smaller gas channel width (20 μm), the resistive loss (green curve) approached the limiting case scenario (black curve). As shown in Fig. 6c, the gas channel width cannot exceed 100 μm to maintain a low (<100 mV) resistive loss for this particular electrode width (2.34 mm). Additional simulations were also performed with the Nafion channel width less than 5.17 μm, which is the upper-bound value that can support the required gas transport. When the Nafion channel width was decreased from 5 μm to 1 μm, the maximum resistive loss showed a weak dependence (<10 mV variation) on the Nafion channel width. As shown in Fig. 6c, as long as the electrode width does not exceed the upper-bound value, various combinations of the Nafion overlayer thickness and the gas channel width can be employed to achieve low resistive losses in Design B.

C. Gas crossover

Fig. 7 shows the percentage of gas crossover due to diffusive transport between the cathode and anode as a function of the electrode width, for three different electrode heights. The gas crossover increased as the width of the electrode decreased. To avoid a gas mixture that contained >4% H_2 in air (the flammability limit), the electrode width must exceed 45.5 μm or 20.2 μm, for an electrode height of 1 μm or 10 μm, respectively. For the 100 μm electrode height, the diffusive gas crossover would not exceed 4% H_2 in air. The convective gas crossovers were therefore inherently minimized in both designs by the use of the Nafion. Due to the small permeability of the Nafion film, $\sim 10^{-18}$ m^2, the convective crossover was negligible in all the designs, even under significant pressure differential, *e.g.*, 1 atm.

IV. Discussion

A. Effect of a lateral conductive layer

A lateral conductive layer has often been proposed and utilized to redistribute the current density and facilitate the ionic transport in the system, by focusing the current density at the edge of a PV-based electrode.[6] In such a system, the majority of the products, hydrogen and oxygen, are generated near the edge of the electrode, and the gases can readily bubble away in a liquid-electrolyte based system. However, use of such a design in a vapor feed system would result in product gases generated underneath the Nafion film, and transported by diffusion of dissolved gas in the membrane. When the current density increases rapidly at the edge of the electrode, the Nafion thickness therefore has to be reduced significantly to accommodate this gas transport. The resulting non-uniform Nafion coating further complicates the resistive losses and electrocatalysis in the system. For example, in Design B, when the electrode width was set to 2.34 mm (Fig. 6), the hydrogen concentration at the electrode edge exceeded the saturation concentration by several orders of magnitude, regardless of any combination of other geometric parameters that were discussed in the previous section. Similarly, in Design A, when the Nafion thickness was set to 1.9 μm, the hydrogen concentration exceeded the saturation concentration at the electrode edge in all cases simulated in Fig. 4. When the Nafion thickness was reduced uniformly to accommodate the high hydrogen flux at the electrode edge, the current density is further focused at the electrode edge, which will result in supersaturation of the gases. For an electrode width >100 μm, no converged solution for a uniform thickness Nafion film was found that could accommodate gas transport at the edges of the electrodes. For an electrode width of <100 μm, at a constant Nafion thickness the maximum resistive loss was comparable (<0.15 mV variation) with or without the lateral conductive layer present.

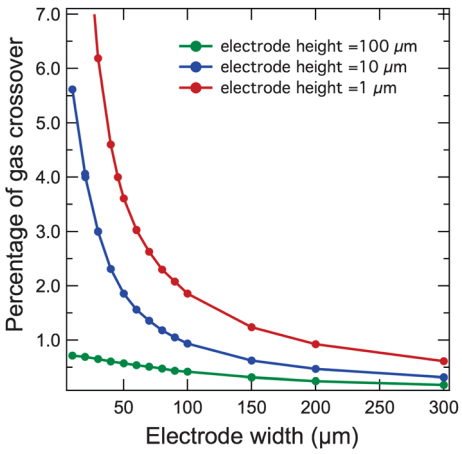

Fig. 7 Percentage of gas crossover as a function of the electrode width when the electrode height was set to 1 μm (red), 10 μm (blue) and 100 μm (green).

B. Comparison to a liquid water device

An integrated photoelectrolysis system that does not have a liquid aqueous electrolyte but that nevertheless is sustained by a liquid water feed has similar design constraints to the systems evaluated herein based on a water vapor feed. However, the use of liquid water as the feedstock has two adverse effects on the system performance: (i) a slightly higher (~44 mV) thermodynamic potential for the water-splitting reaction as compared to a vapor-fed device, (ii) formation of bubbles at the Nafion/water interface. Moreover, an integrated system based on a liquid water feed or that contains a liquid aqueous electrolyte generally requires a relatively high-purity water solution to minimize contamination or corrosion of functional components (photoabsorbers, electrocatalysts, *etc.*). However, in a device fed by water vapor, the low purity water can be distilled to produce the steam or can be evaporated to produce the needed humidity, provided that the device assembly is not in physical contact with the low purity water source. Of course, the transport properties of a Nafion film can vary significantly in contact with different water sources, and such variations will alter somewhat the precise values of the optimum design parameters relative to those presented herein.

C. Comparison to an electrically connected PV and MEA design

A solar-driven water-splitting system sustained by a water vapor feed can also be realized by electrically connecting a PV unit to a membrane-electrode assembly (MEA). The MEA would then essentially operate as a fuel cell in reverse, in which the water vapor is the feedstock for the cathode and anode, and the photovoltage provided by the PV serves as the driving force for the electrolysis reaction. Detailed comparisons between an integrated photoelectrolysis device and a discrete PV + MEA system, for different band gap combinations of photoabsorbers[8] and various cell operating environments (irradiation and temperature), have been recently presented.[7] The integrated photoelectrolysis system leverages enhanced kinetics and transport at elevated temperatures, and therefore would outperform a discrete PV unit connected electrically to a discrete electrolysis system.[7] Moreover, an integrated photoelectrolysis system permits the use of a semiconductor/electrolyte junction, in which a single photoabsorber material serves as the photocathode or anode in contact with electrolyte solution, in contrast to a standalone PV + MEA system in which a "buried" junction is required.

V. Conclusions

Detailed geometric parameters in two cell designs were investigated in this study for a photoelectrolysis system sustained by a water vapor feed. In Design A, the thickness of the Nafion film cannot exceed 1.9 μm to accommodate the product gas transport, and the width of the photoelectrode cannot exceed ~300 μm, to hold the resistive losses in the system to acceptable levels. In Design B, the maximum electrode width can be significantly increased, to ~4.5 mm by employing a structured Nafion film, for which the width of the Nafion channel cannot exceed 5.17 μm to accommodate the required transport of the product gases. To prevent significant diffusive gas crossover (4%) for micro-sized electrodes, the width of the electrode has to exceed 45.5 μm or 20.2 μm, respectively for electrode heights of 1 μm or 10 μm, respectively. A lateral conductive layer, typically employed to lower the resistive loss in a photoelectrolysis system based on a liquid electrolyte, is unfavorable in a water vapor device, due to enhanced current densities at the electrode edges that cause supersaturation of product gases in the system.

The design principles investigated herein can be applied to both a water vapor based device and to a pure water based device, in which the use of strongly alkaline or acidic liquid electrolytes is eliminated. Large-scale implementation of a photoelectrolysis system can benefit from the use of water vapor or pure water as the feedstock. Optimal electron, ion and gas transport in such a device can be realized either by decreasing the width of the photoelectrode or by employing a complex proton- and gas-transport structure. Although both designs can achieve the same reactant/product transport as well as produce similar resistive losses, Design A is more suitable for photoelectrode materials that can be readily fabricated into microelectrodes and Design B is more suitable for macro-scale photovoltaic electrodes.

Acknowledgements

This material is based upon work performed by the Joint Center for Artificial Photosynthesis, a DOE Energy Innovation Hub, supported through the Office of Science of the U.S. Department of Energy under Award number DE-SC0004993.

References

1 N. S. Lewis, Toward cost-effective solar energy use, *Science*, 2007, **315**(5813), 798–801.
2 N. S. Lewis and D. G. Nocera, Powering the planet: Chemical challenges in solar energy utilization, *Proc. Natl. Acad. Sci. U. S. A.*, 2007, **104**(50), 20142.
3 M. G. Walter, E. L. Warren, J. R. McKone, S. W. Boettcher, Q. X. Mi, E. A. Santori and N. S. Lewis, Solar Water Splitting Cells, *Chem. Rev.*, 2010, **110**(11), 6446–6473.
4 C. X. Xiang, G. M. Kimball, R. L. Grimm, B. S. Brunschwig, H. A. Atwater and N. S. Lewis, 820 mV open-circuit voltages from Cu_2O/CH_3CN junctions, *Energy Environ. Sci.*, 2011, **4**(4), 1311–1318.
5 C. X. Xiang, A. C. Meng and N. S. Lewis, Evaluation and optimization of mass transport of redox species in silicon microwire-array photoelectrodes, *Proc. Natl. Acad. Sci. U. S. A.*, 2012, **109**(39), 15622–15627.
6 S. Haussener, C. X. Xiang, J. M. Spurgeon, S. Ardo, N. S. Lewis and A. Z. Weber, Modeling, simulation, and design criteria for photoelectrochemical water-splitting systems, *Energy Environ. Sci.*, 2012, **5**(12), 9922–9935.
7 S. Haussener, S. Hu, C. Xiang, A. Z. Weber and N. Lewis, Simulations of the irradiation and temperature dependence of the efficiency of tandem photoelectrochemical water-splitting systems, *Energy Environ. Sci.*, 2013, DOI: 10.1039/C3EE41302K.
8 S. Hu, C. Xiang, S. Haussener, A. D. Berger and N. S. Lewis, An analysis of the optimal band gaps of light absorbers in integrated tandem photoelectrochemical water-splitting systems, *Energy Environ. Sci.*, 2013, **6**, 2984–2993.
9 S. Y. Reece, J. A. Hamel, K. Sung, T. D. Jarvi, A. J. Esswein, J. J. H. Pijpers and D. G. Nocera, Wireless Solar Water Splitting Using Silicon-Based Semiconductors and Earth-Abundant Catalysts, *Science*, 2011, **334**(6056), 645–648.
10 J. Suntivich, K. J. May, H. A. Gasteiger, J. B. Goodenough and Y. Shao-Horn, A Perovskite Oxide Optimized for Oxygen Evolution Catalysis from Molecular Orbital Principles, *Science*, 2011, **334**(6061), 1383–1385.
11 S. W. Boettcher, E. L. Warren, M. C. Putnam, E. A. Santori, D. Turner-Evans, M. D. Kelzenberg, M. G. Walter, J. R. McKone, B. S. Brunschwig, H. A. Atwater and N. S. Lewis, Photoelectrochemical Hydrogen Evolution Using Si Microwire Arrays, *J. Am. Chem. Soc.*, 2011, **133**(5), 1216–1219.
12 Y. J. Zhang, C. Wang, N. F. Wan, Z. X. Liu and Z. Q. Mao, Study on a novel manufacturing process of membrane

electrode assemblies for solid polymer electrolyte water electrolysis, *Electrochem. Commun.*, 2007, **9**(4), 667–670.

13 S. A. Grigoriev, V. I. Porembsky and V. N. Fateev, Pure hydrogen production by PEM electrolysis for hydrogen energy, *Int. J. Hydrogen Energy*, 2006, **31**(2), 171–175.

14 O. Khaselev and J. A. Turner, A monolithic photovoltaic-photoelectrochemical device for hydrogen production via water splitting, *Science*, 1998, **280**(5362), 425–427.

15 S. Licht, B. Wang, S. Mukerji, T. Soga, M. Umeno and H. Tributsch, Efficient solar water splitting, exemplified by RuO_2-catalyzed AlGaAs/Si photoelectrolysis, *J. Phys. Chem. B*, 2000, **104**(38), 8920–8924.

16 M. Philippe, H. Jerome, B. Sebastien and P. Gerard, Modelling and calculation of the current density distribution evolution at vertical gas-evolving electrodes, *Electrochim. Acta*, 2005, **51**(6), 1140–1156.

17 J. Eigeldinger and H. Vogt, The bubble coverage of gas-evolving electrodes in a flowing electrolyte, *Electrochim. Acta*, 2000, **45**(27), 4449–4456.

18 L. J. J. Janssen and S. J. D. Vanstralen, Bubble Behavior on and Mass-Transfer to an Oxygen-Evolving Transparent Nickel Electrode in Alkaline-Solution, *Electrochim. Acta*, 1981, **26**(8), 1011–1022.

19 A. W. Bryson and D. L. Hofman, A Population Balance Approach to the Study of Bubble Behavior at Gas-Evolving Electrodes, *J. Appl. Electrochem.*, 1989, **19**(1), 116–119.

20 A. J. Bard and L. R. Faulkner, *Electrochemical Methods, Fundamentals and Applications*, Wiley, 2nd edn, 2000.

21 J. M. Spurgeon and N. S. Lewis, Proton exchange membrane electrolysis sustained by water vapor, *Energy Environ. Sci.*, 2011, **4**(8), 2993–2998.

22 J. Newman and K. Thomas-Alyea, *Electrochemical Systems*, Wiley & Sons, 2004.

23 K. J. Vetter, *Electrochemical Kinetics*, Academic Press, 1963.

24 C. C. McCrory, S. L. Jung and T. F. Jaramillo, Benchmarking Heterogeneous Electrocatalysts for the Oxygen Evolution Reaction, *J. Am. Chem. Soc.*, 2013, submitted for publication.

25 A. Z. Weber and J. Newman, Transport in polymer-electrolyte membranes – I. Physical model, *J. Electrochem. Soc.*, 2003, **150**(7), A1008–A1015.

26 A. Z. Weber and J. Newman, Transport in polymer-electrolyte membranes – III. Model validation in a simple fuel-cell model, *J. Electrochem. Soc.*, 2004, **151**(2), A326–A339.

27 A. Z. Weber and J. Newman, Transport in polymer-electrolyte membranes – II. Mathematical model, *J. Electrochem. Soc.*, 2004, **151**(2), A311–A325.

28 W. M. Haynes, *CRC Handbook of Chemistry and Physics*, 94th edn, 2013.